Volume 6 | Number 14 | 21 July 2014 | Pages 7677–8406

Nanoscale

www.rsc.org/nanoscale

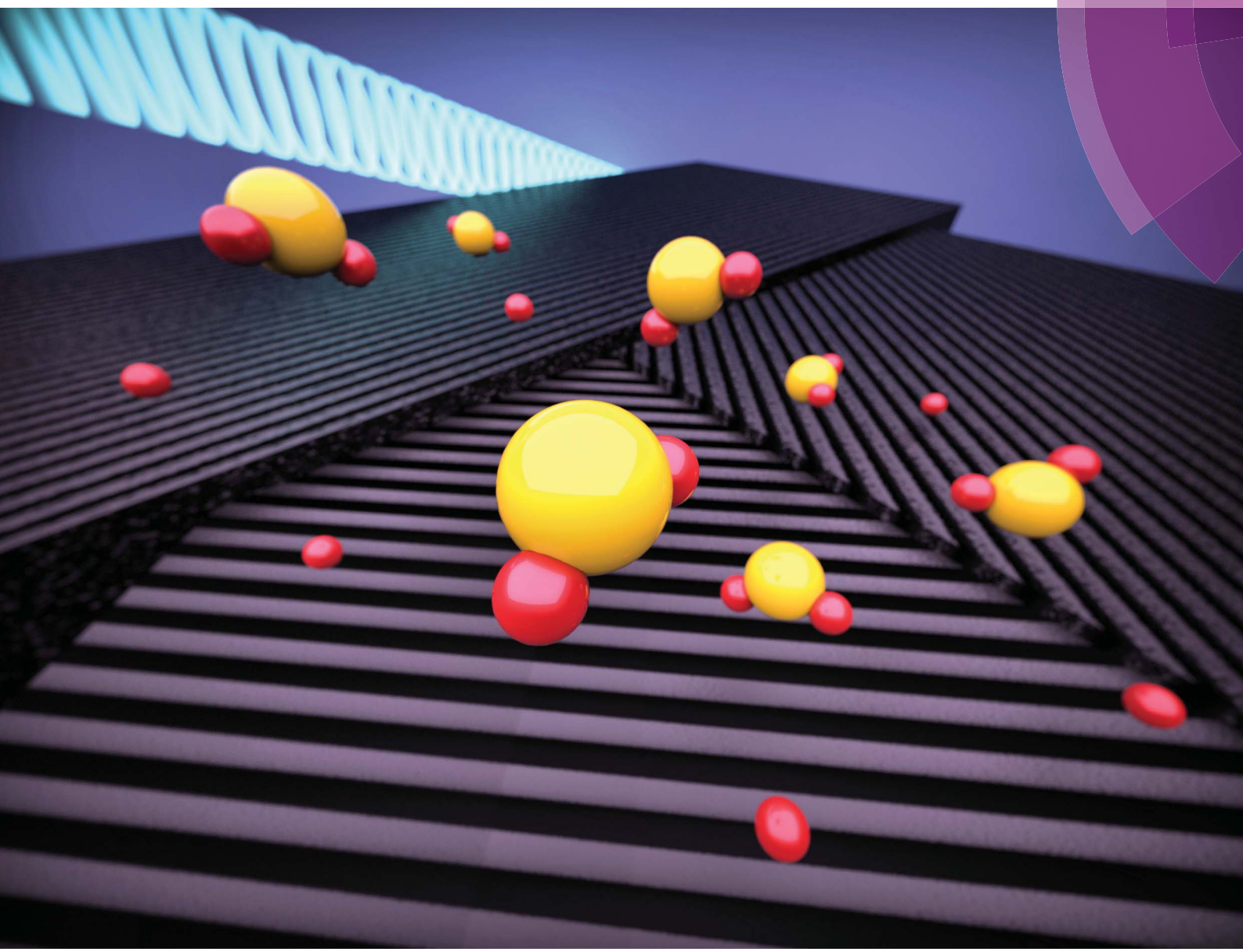

ISSN 2040-3364

ROYAL SOCIETY OF CHEMISTRY

COMMUNICATION

Yu-Lun Chueh *et al.*

Fabrication of large-scale single-crystal bismuth telluride (Bi_2Te_3) nanosheet arrays by a single-step electrolysis process

NCNST

Nanoscale

COMMUNICATION

View Article Online
View Journal | View Issue

Cite this: *Nanoscale*, 2014, **6**, 7780

Received 11th January 2014
Accepted 21st March 2014

DOI: 10.1039/c4nr00184b

www.rsc.org/nanoscale

Fabrication of large-scale single-crystal bismuth telluride (Bi_2Te_3) nanosheet arrays by a single-step electrolysis process†

Hung-Wei Tsai,[a] Tsang-Hsiu Wang,[a] Tsung-Cheng Chan,[a] Pei-Ju Chen,[a] Chih-Chun Chung,[b] Alireza Yaghoubi,[c] Chien-Neng Liao,[a] Eric Wei-Guang Diau[b] and Yu-Lun Chueh*[ad]

Nanolizing of thermoelectric materials is one approach to reduce the thermal conductivity and hence enhance the figure of merit. Bismuth telluride (Bi_2Te_3)-based materials have excellent figure of merit at room temperature. For device applications, precise control and rapid fabrication for the nanostructure of thermoelectric materials are essential issues. In the present study, we demonstrate a one-step electrolysis process to directly form Bi_2Te_3 nanosheet arrays (NSAs) on the surface of bulk Bi_2Te_3 with controllable spacing distance and depth by tuning the applied bias and duration. The single sheet of NSAs reveals that the average thickness and electrical resistivity of single crystalline Bi_2Te_3 in composition are 399.8 nm and 137.34 μΩ m, respectively. The formation mechanism of NSAs has been proposed. A 1.12% efficiency of quantum dot-sensitized solar cells with Bi_2Te_3 NSAs for counter electrode has been demonstrated, indicating that Bi_2Te_3 NSAs from top-down processing with a high ratio of surface area to volume are a promising candidate for possible applications such as thermoelectrics, dye-sensitized solar cells (DSSCs), and lithium-ion batteries.

1. Introduction

Two-dimensional materials[1] such as graphite,[2] h-BN,[3] MoS_2,[4] and Bi_2Te_3 [5] have the van der Waals gap in their crystal structure. Because of the weak van der Waals force, two-dimensional materials can be exfoliated to nanosheets by mechanical cleavage methods. Furthermore, metal ions can be intercalated into the van der Waals gap of these two-dimensional materials and thus form nanosheets.[6] In recent years, Bi_2Te_3-based materials have attracted much attention due to their interesting physical properties. For example, nanostructured Bi_2Te_3 with a high surface area has been used in dye-sensitized solar cells (DSSCs)[7] and lithium-ion batteries.[8] In addition, nanostructured Bi_2Te_3 comes with a high thermoelectric figure of merit, namely ZT value, which is used to examine the thermoelectric performance of a thermoelectric material.[9] The dimensionless figure of merit (ZT) can be given by $ZT = (S^2\sigma/\kappa)T$ where S, σ, κ, and T are the Seebeck coefficient (μV K^{-1}), electrical conductivity (Ω^{-1} m^{-1}), thermal conductivity (W m^{-1} K^{-1}), and temperature (K), respectively. The ZT value of the nanostructured thermoelectric materials can be enhanced as thermal conductivity decreases as reported by both experimental[10] and theoretical[11] works. Therefore, it is an important issue to control the nanostructure of thermoelectric materials precisely.

The quintuple layer (QL) of the Bi_2Te_3 consists of five monoatomic sheets ($Te^{(1)}$–Bi–$Te^{(2)}$–Bi–$Te^{(1)}$), which are obtained by mechanical exfoliation or metal ion intercalation. Significantly decreased thermal conductivity of the QL of Bi_2Te_3 was observed.[12] For high production yield and size uniformity of Bi_2Te_3 nanosheets, hydrothermal synthesis and the electrochemical method are suitable methods for mass production.[9,13] Although nanoplates, nanowires, nanotubes, and nanodots can be obtained by a hydrothermal method, a complicated device fabrication process is needed. In contrast to the hydrothermal method, the electrochemical method is a proper way to achieve mass production for thermoelectric device applications. For example, a large area of arranged Bi_2Te_3 nanowires was obtained by electrodepositing Bi_2Te_3 into an anodic aluminum oxide (AAO) template with enhanced thermoelectric properties.[13] However, post-treatments such as removal of AAO or transfer processing of arranged Bi_2Te_3 NWs for device applications may be needed.

To the best of our knowledge, rapid fabrication of a large scale Bi_2Te_3 nanostructure has not yet been explored. The electrochemical method is a non-vacuum process and comes with advantages of large scale and low-cost fabrication. In this

[a]*Department of Materials Science and Engineering, National Tsing Hua University, Hsinchu, 30013, Taiwan*

[b]*Department of Applied Chemistry, National Chiao Tung University, Hsinchu 30010, Taiwan*

[c]*Centre for High Impact Research, University of Malaya, Kuala Lumpur 50603, Malaysia*

[d]*Center for Nanotechnology, Material Science, and Microsystem, National Tsing Hua University, Hsinchu, 30013, Taiwan. E-mail: ylchueh@mx.nthu.edu.tw*

† Electronic supplementary information (ESI) available. See DOI: 10.1039/c4nr00184b

regard, we demonstrate a one-step electrochemical method to fabricate large-scale single-crystal Bi_2Te_3 nanosheet arrays (NSAs) on the surface of bulk Bi_2Te_3. We have found that the area of Bi_2Te_3 NSAs depends on the plane directions of Bi_2Te_3 grains and the depth of Bi_2Te_3 NSAs relies on the applied bias and duration. Phase structures and microstructures were characterized by X-ray diffraction, Raman spectroscopy, and transmission electron microscopy (TEM). In addition, the physical properties, such as thickness and resistivity, of single Bi_2Te_3 nanosheets were measured and investigated in detail. A formation mechanism of NSAs has been proposed. Finally, the possible replacement of counter electrodes for DSSCs has been demonstrated.

2. Experimental section

Fabrication of Bi_2Te_3 NSAs

Bismuth (99.99 wt%, ADMAT) and tellurium (99.999 wt%, ADMAT) were used without further purification. Dilute nitric acid with a pH level of 1.2 was used as an electrolyte in the one-step electrochemical method with a three-electrode system for bias control. Because of compensation for evaporation of Te at high-temperature processing, additional Te (3 wt%) was added for the synthesis of the stoichiometric Bi_2Te_3 compound. The weighed Bi and Te ingots were sealed in an evacuated quartz tube and annealed in a furnace at 850 °C for 48 h for synthesis of bulk Bi_2Te_3. Subsequently, the synthesized bulk Bi_2Te_3 samples were sliced into circular disks with 1 cm in diameter and 3 mm in thickness. The polished bulk Bi_2Te_3 was used as a working electrode in which the mercury/mercury chloride (Hg/Hg_2Cl_2) electrode and platinum electrode were used as the reference electrode and counter electrode, respectively. The Bi_2Te_3 NSAs with a periodic spacing distance of ~1 μm and tens of micrometers in depth were formed while various biases were applied for a few seconds to a few minutes.

Device fabrication

For the electrical measurements, the Bi_2Te_3 nanosheet was put on a 50 nm thick SiO_2/Si substrate, followed by dropping the sample into diluted nitric acid to remove the native oxide. A 150 nm thick Ni metal layer was deposited by electron beam deposition as electrodes and defined by a photolithography process. For the CdSe QD-SSC fabrication, the TiO_2 films were prepared by screen printing of TiO_2 paste on FTO glass and sintering to form TiO_2 mesoporous electrode. Chemical bath deposition was used to assemble CdSe QDs onto the TiO_2 electrode, and then the TiO_2/CdSe electrode was sandwiched with Bi_2Te_3 NSAs, pure FTO, and Pt as counter electrodes for further photovoltaic property measurements after injecting the polysulfide as an electrolyte. The active area of the cell was 0.16 cm^2.

Characterization

The crystallization and compositions of Bi_2Te_3 were confirmed by X-ray diffraction (Shimadzu XRD 6000, CuKα radiation with a wavelength of 0.154 nm) and micro-Raman spectrometry (632.8 nm He–Ne laser with a laser intensity of 2 mW). Scanning electron microscopy (JSM 6500-F, JOEL operated at 15 kV with a resolution of 3.0 nm) and field-emission transmission electron microscopy (JEM-3000F, JEOL operated at 300 kV with a point-to-point resolution of 0.17 nm) were used to obtain the microstructures and compositions. The electrical properties were measured using a Agilent B1500A semiconductor parameter analyzer at room temperature.

3. Results and discussion

Fig. 1 shows a schematic of how we fabricated Bi_2Te_3 NSAs with a periodic spacing distance of ~1 μm and tens of micrometers in depth at various biases for a few seconds to a few minutes. Bulk Bi_2Te_3 was first prepared by sintering Bi and Te powders together, and then as-prepared bulk Bi_2Te_3 was polished until the surface appeared to have a metallic luster as shown in Fig. 1(a). Fig. 1(b) shows a schematic of the three-electrode system, which was used to fabricate Bi_2Te_3 NSAs. The polished Bi_2Te_3 bulk was used as a working electrode. The mercury/mercury chloride (Hg/Hg_2Cl_2) electrode and platinum electrode were used as the reference electrode and counter electrode, respectively. After applying a negative bias on the working electrode, Bi_2Te_3 NSAs were formed on the surface of bulk Bi_2Te_3 as shown in Fig. 1(c). The corresponding scanning electron microscopy (SEM) image is shown in Fig. 1(d), in which we could observe Bi_2Te_3 NSAs formed on the allowed plane direction grains in the upper part and lower-left part. Note that no Bi_2Te_3 NSAs were formed on the forbidden plane direction grains in the lower-right part. The inset shows a higher magnification image of a single Bi_2Te_3 layer captured from the rectangular area in Fig. 1(d).

After the electrochemical treatment, the bulk Bi_2Te_3 bulk was immersed in deionized water to remove the electrolyte. The

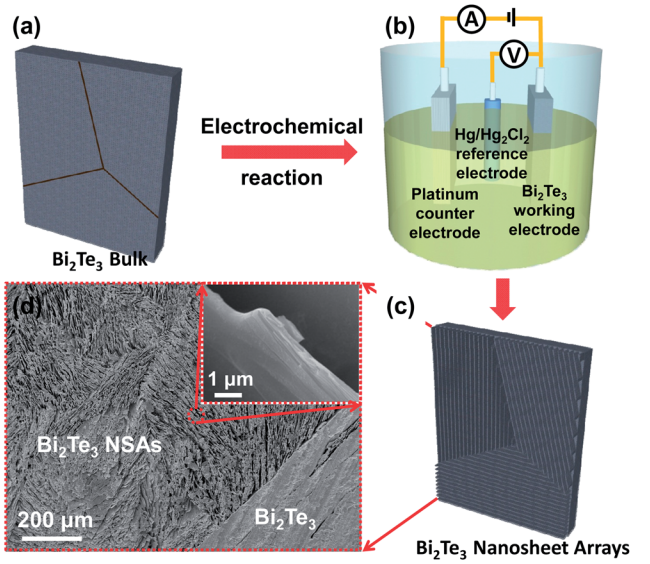

Fig. 1 Schematics of the experimental flow chart and SEM images. (a) Bulk Bi_2Te_3. (b) The three-electrode system. (c) Bi_2Te_3 NSAs. (d) SEM image of Bi_2Te_3 NSAs and a higher magnification image (inset).

Bi_2Te_3 NSAs coincided with rhombohedral Bi_2Te_3 (JCPDS 89-4302) in the XRD spectrum as well as the bulk Bi_2Te_3 without formation of NSAs as shown in Fig. 2(a). Moreover, the single Bi_2Te_3 sheet was examined by using direct sonication of Bi_2Te_3 NSAs in ethanol for comparison. The corresponding Raman spectra and transmission electron microscopy (TEM) image of the single Bi_2Te_3 sheet are shown in Fig. 2(b)–(d). For the Raman spectra of a single Bi_2Te_3 sheet, two main peaks at 102.4 and 133.2 cm^{-1} were observed, which are attributed to optical modes of $2E_g$ and $2A_{1g}$, respectively.[14] These two main optical mode peaks are consistent with the Raman spectra of the pristine Bi_2Te_3 bulk (Fig. 2(b)). The Fig. 2(c) shows a TEM image of a Bi_2Te_3 sheet. The dark lines observed in the Bi_2Te_3 sheet are probably due to the dislocations inside. The inset in Fig. 2(c) shows the corresponding selected area diffraction pattern (SAD). Obviously, symmetric spots indicate a single crystalline feature of the Bi_2Te_3 sheet. According to zone axis of the electron diffraction pattern, the plane direction of the Bi_2Te_3 sheet is (001), which is very important for understanding the formation mechanism of Bi_2Te_3 NSAs. The high-resolution TEM (HRTEM) image shown in Fig. 2(d) is in agreement with the Bi_2Te_3 (110) plane, where a lattice spacing of 0.218 nm was indexed.

Fig. 3(a) shows that the unit cell of the Bi_2Te_3 consisted of fifteen monoatomic sheets of bismuth and tellurium atoms in the rhombohedral crystalline structure. The bonding states between Bi–$Te^{(1)}$ and Bi–$Te^{(2)}$ are different and are attributed to ionic and covalent bonds, respectively. It is reported by Drabble and Goodman that these bonds are much stronger than the van der Waals force ($Te^{(1)}$–$Te^{(1)}$).[15] To shed light on the formation mechanism of the Bi_2Te_3 NSAs, the *ex situ* formation of Bi_2Te_3 NSAs was observed at the applied bias of −2 V with different duration of 5, 15, and 30 s as shown in Fig. 3(b). The corresponding schematics of the formation processes of Bi_2Te_3 NSAs are also shown in Fig. 3(c). With increasing duration, the bulk Bi_2Te_3 was etched away and formed Bi_2Te_3 NSAs during the electrolysis process. The reactivity sites of Bi_2Te_3 under applied bias can be examined by the Bi–Te bond energy. Kaviany and coworkers reported the bond energies of $Te^{(1)}$–Bi, $Te^{(2)}$–Bi, and $Te^{(1)}$–$Te^{(1)}$ in Bi_2Te_3 to be 0.974, 0.5801, and 0.0691 eV, respectively, by using computational methods.[16] As seen in Fig. 3(a), a $Te^{(1)}$ atom binds with three Bi and three $Te^{(1)}$ atoms. As a result, it needs 3.1293 eV to release a $Te^{(1)}$ atom (for detailed calculation, please see the ESI†). For a $Te^{(2)}$ atom binding with six Bi atoms, it needs 3.4806 eV to release a $Te^{(2)}$ atom (for detailed calculation, please see the ESI†). However, it needs 4.6623 eV to release a Bi atom from three Bi–$Te^{(1)}$ bonds and three Bi–$Te^{(2)}$ bonds (for detailed calculation, please see the ESI†). Therefore, the $Te^{(1)}$ atom is the easiest to be removed because of its weak bonding energy. Besides, the distance between two monoatomic sheets of $Te^{(1)}$–$Te^{(1)}$ is 2.598 Å, and the diameter of a hydrogen atom can be considered as two times the Bohr radius (1.058 Å), which is smaller than the gap of the $Te^{(1)}$–$Te^{(1)}$.[17] Therefore, hydrogen ions can be easily inserted into the gap of the $Te^{(1)}$–$Te^{(1)}$ and thus react with $Te^{(1)}$ atoms to produce H_2 and H_2Te gases during the electrolysis process. For better understanding, we designed an experiment to prove the existence of H_2Te gas by observing the H_2Te-derived tellurium blade on the surface of a suspended silicon substrate (details in ESI†). Once $Te^{(1)}$ atoms are etched, the Bi_2Te_3 NSAs can be formed along the (001) surface of the bulk Bi_2Te_3. The etching processes of Bi_2Te_3 are shown in Fig. 3(c).

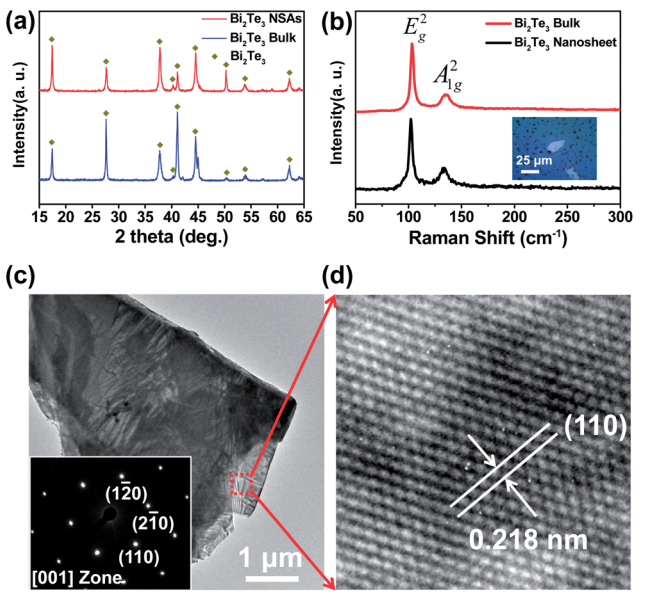

Fig. 2 Material analysis for Bi_2Te_3 NSAs. (a) XRD spectra of bulk Bi_2Te_3 w/ and w/o NSAs. (b) Raman spectra of a Bi_2Te_3 nanosheet and bulk Bi_2Te_3. (c) TEM image of a Bi_2Te_3 nanosheet. The inset shows the corresponding diffraction pattern. (d) High-resolution TEM image of Bi_2Te_3 nanosheet taken from (c).

To understand the spacing control of the Bi_2Te_3 NSAs, different biases were applied, for which the total charge flux for each applied bias was fixed. The spacing distances of Bi_2Te_3 NSAs as a function of various applied biases were plotted as shown in Fig. 4(a). The electrolysis parameters and SEM images of the Bi_2Te_3 NSAs for various applied biases are shown in Table 1 and Fig. 4(b)–(f), respectively. Obviously, the spacing distance is slightly decreased as the applied bias increases, suggesting that more reaction sites are created under the larger applied bias. The corresponding relationship between spacing distance and applied bias could be described by the following fitted curve:

$$y = -0.161 \times \ln(-x) + 1.4333$$

where y is the spacing distance and x is the applied bias. To measure the electrical properties of Bi_2Te_3 nanosheets, a conventional photolithography technique was used to prepare two-terminal devices, and the corresponding thicknesses of the Bi_2Te_3 nanosheets were measured by atomic force microscopy (AFM). Then, the measured thickness of the Bi_2Te_3 nanosheet was used for resistivity calculation as shown in Fig. 5, the inset of which shows the corresponding device configuration. Consequently, the average thickness and electrical resistivity of the Bi_2Te_3 nanosheets are ~399.8 nm and ~137.34 μΩ m, respectively. The electrical resistivity of the Bi_2Te_3 nanosheets is

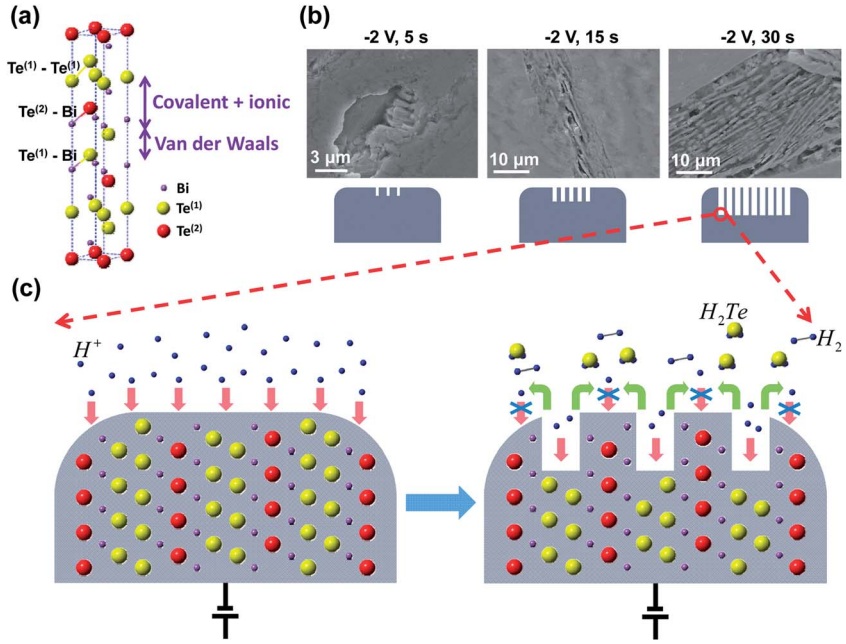

Fig. 3 Schematic of the mechanism of Bi_2Te_3 NSA formation. (a) Unit cell of Bi_2Te_3. (b) Formation schematic of Bi_2Te_3 NSAs at different steps and corresponding SEM images. (c) Schematic of how the hydrogen ion reacts with Bi_2Te_3 and forms Bi_2Te_3 NSAs.

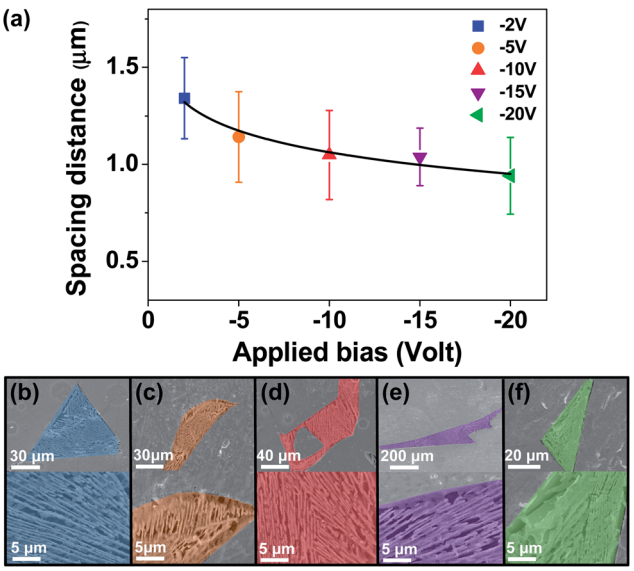

Fig. 4 (a) Spacing distances of Bi_2Te_3 NSAs under different applied biases and (b–f) their corresponding SEM images. The top panels are low-magnification images, and the bottom panels are high-magnification images.

Table 1 Electrolysis parameters at various applied biases

Applied bias (voltage)	−2	−5	−10	−15	−20
Duration (s)	300	120	60	45	30

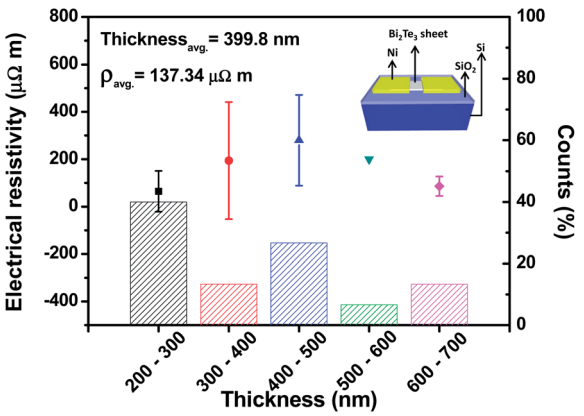

Fig. 5 Electrical property statistics of Bi_2Te_3 nanosheets and schematic of electronic device (inset).

larger than that in a previous work[18] by one order of magnitude, which may be the result of contact resistance owing to two-terminal measurement and doping conditions during synthesis of Bi_2Te_3.[19] These two reasons can result in an increased measured resistance of the Bi_2Te_3 nanosheet.

Generally, platinum (Pt) is used as a counter electrode for quantum dot-sensitized solar cells (QD-SSCs). However, Pt is an expensive and rare material in the world. Some alternative materials for the counter electrode have been proposed, such as metal chalcogenide,[20,21] Au,[22] and carbon.[23] The metallic property due to a very low band gap of ~0.15 eV [24] and matched electron affinity of ~4.125–4.525 eV [25] make Bi_2Te_3 NSAs a potential candidate as the counter electrode to replace Pt for possible application in QD-SSCs. To shed light on this part, Fig. (6) shows the current density–voltage (J–V) curves of CdSe QD-SSCs with Bi_2Te_3 NSAs, pure FTO, and Pt as counter electrodes under 1 sun illumination. The photovoltaic (PV) properties of these electrodes are listed in Table 2. As can be seen in

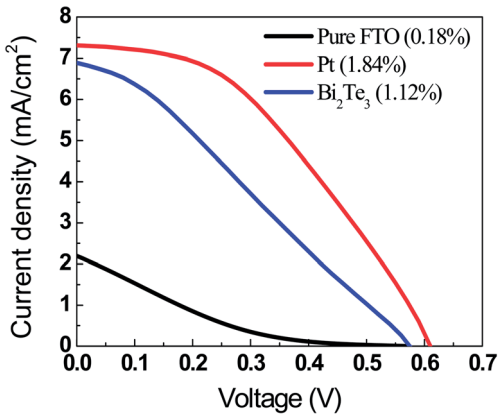

Fig. 6 *J–V* characteristic of CdSe QD-SSCs with three different counter electrodes (Bi_2Te_3 NSAs, pure FTO, and Pt).

Table 2 Photovoltaic properties of QD-SSCs

Electrode	V_{oc} (V)	J_{sc} (mA cm^{-2})	FF	η (%)	Ref.
TiO_2/CdSe, Pt	0.62	7.31	0.41	1.84	This work
TiO_2/CdSe, Pt	0.65	4.65	0.31	0.90	26
TiO_2/CdSe, Pt	0.68	6.03	0.39	1.60	26
TiO_2/CdSe, Pt	0.46	8.70	0.31	1.24	27
TiO_2/CdSe, Pt	0.65	3.27	0.50	1.08	28
TiO_2/CdSe, Pt	0.61	3.93	0.49	1.19	28
TiO_2/CdSe, Bi_2Te_3 NSAs	0.58	6.89	0.28	1.12	This work
TiO_2/CdSe, FTO	0.57	2.20	0.14	0.18	This work

Table 2, the open-circuit voltage (V_{oc}) of the Bi_2Te_3 counter electrode is 0.581 V, which is lower than that of the Pt electrode by 0.035 V. The short-circuit current (J_{sc}) of the Bi_2Te_3 NSAs and Pt counter electrodes are 6.891 and 7.314 mA cm^{-2}, respectively. Therefore, the PV conversion efficiency of the Bi_2Te_3 NSAs as the counter electrode can reach 1.12%, which is better than that of the device using pure FTO as the electrode (0.18%) and comparable with that of Pt as the counter electrode (0.9–1.84%).

4. Conclusions

We have demonstrated a novel one-step electrolysis process for directly fabricating large-scale Bi_2Te_3 NSAs. The composition and properties of Bi_2Te_3 NSAs have been analyzed by XRD, Raman spectroscopy, SEM, TEM, and electrical measurements. The spacing distance and depth of Bi_2Te_3 NSAs depend on the applied bias, current densities and bias duration. Our experimental results indicate that the spacing distance of Bi_2Te_3 nanosheets is of 1 μm with a thickness of several hundred nanometers. Moreover, the Bi_2Te_3 NSAs show potential for a wide variety of applications due to the high surface area to volume ratio. The formation mechanism of Bi_2Te_3 NSAs was proposed as well. The Bi_2Te_3 NSAs as counter electrodes of CdSe QD-SSCs with a PV conversion efficiency of 1.12% have been demonstrated. The proposed process may be used for the synthesis of other NSAs employing different materials such as Sb_2Te_3 and $MoSe_2$ in future.

Acknowledgements

The research was supported by the National Science Council through Grant nos NSC 101-2112-M-007-015-MY3, 101-2218-E-007-009-MY3, and 102-2633-M-007-002, and the National Tsing Hua University through Grant no. 102N2022E1. Y. L. Chueh greatly appreciates the use of facilities at CNMM, National Tsing Hua University through Grant no. 102N2744E1.

References

1 M. Xu, T. Liang, M. Shi and H. Chen, *Chem. Rev.*, 2013, **113**, 3766.
2 K. S. Novoselov, A. K. Geim, S. V. Morozov, D. Jiang, Y. Zhang, S. V. Dubonos, I. V. Grigorieva and A. A. Firsov, *Science*, 2004, **306**, 666.
3 Y. Lin, T. V. Williams and J. W. Connell, *J. Phys. Chem. Lett.*, 2009, **1**, 277.
4 V. Stengl and J. Henych, *Nanoscale*, 2013, **5**, 3387.
5 D. Teweldebrhan, V. Goyal and A. A. Balandin, *Nano Lett.*, 2010, **10**, 1209.
6 Z. Ding, S. K. Bux, D. J. King, F. L. Chang, T.-H. Chen, S.-C. Huang and R. B. Kaner, *J. Mater. Chem.*, 2009, **19**, 2588.
7 T. Chen, G. H. Guai, C. Gong, W. Hu, J. Zhu, H. Yang, Q. Yan and C. M. Li, *Energy Environ. Sci.*, 2012, **5**, 6294.
8 F. Tu, J. Xie, G. Cao and X. Zhao, *Materials*, 2012, **5**, 1275.
9 R. J. Mehta, Y. Zhang, C. Karthik, B. Singh, R. W. Siegel, T. Borca-Tasciuc and G. Ramanath, *Nat. Mater.*, 2012, **11**, 233–240.
10 V. Goyal, D. Teweldebrhan and A. A. Balandin, *Appl. Phys. Lett.*, 2010, **97**, 133117.
11 A. Balandin and K. L. Wang, *J. Appl. Phys.*, 1998, **84**, 6149.
12 B. Qiu and X. Ruan, *Appl. Phys. Lett.*, 2010, **97**, 183107.
13 C.-L. Chen, Y.-Y. Chen, S.-J. Lin, J. C. Ho, P.-C. Lee, C.-D. Chen and S. R. Harutyunyan, *J. Phys. Chem. C*, 2010, **114**, 3385.
14 W. Richter and C. R. Becker, *Phys. Status Solidi B*, 1977, **84**, 619.
15 J. R. Drabble and C. H. L. Goodman, *J. Phys. Chem. Solids*, 1958, **5**, 142.
16 B.-L. Huang and M. Kaviany, *Phys. Rev. B: Condens. Matter Mater. Phys.*, 2008, **77**, 125209.
17 W. Kullmann, J. Geurts, W. Richter, N. Lehner, H. Rauh, U. Steigenberger, G. Eichhorn and R. Geick, *Phys. Status Solidi B*, 1984, **125**, 131.
18 H. J. Goldsmid, *Proc. Phys. Soc.*, 1958, **71**, 633.
19 J. P. Fleurial, L. Gailliard, R. Triboulet, H. Scherrer and S. Scherrer, *J. Phys. Chem. Solids*, 1988, **49**, 1237–1247.
20 Z. Tachan, M. Shalom, I. Hod, S. Rühle, S. Tirosh and A. Zaban, *J. Phys. Chem. C*, 2011, **115**, 6162.
21 Z. Yang, C.-Y. Chen, C.-W. Liu, C.-L. Li and H.-T. Chang, *Adv. Energy Mater.*, 2011, **1**, 259.

22 G. Sixto, M.-S. Iván, M. Lorena, G. Nestor, L.-V. Teresa, G. Roberto, J. D. Lina, S. Qing, T. Taro and B. Juan, *Nanotechnology*, 2009, **20**, 295204.
23 M. Seol, E. Ramasamy, J. Lee and K. Yong, *J. Phys. Chem. C*, 2011, **115**, 22018.
24 S. K. Mishra, S. Satpathy and O. Jepsen, *J. Phys.: Condens. Matter*, 1997, **9**, 461.
25 J. Nagao, E. Hatta and K. Mukasa, *The 15th International Conference on Thermoelectrics*, 1996, pp. 404–407.
26 L. J. Diguna, Q. Shen, J. Kobayashi and T. Toyoda, *Appl. Phys. Lett.*, 2007, **91**, 023116.
27 Y.-L. Lee and Y.-S. Lo, *Adv. Funct. Mater.*, 2009, **19**, 604.
28 H. Lee, M. Wang, P. Chen, D. R. Gamelin, S. M. Zakeeruddin, M. Grätzel and M. K. Nazeeruddin, *Nano Lett.*, 2009, **9**, 4221.